CHARACTERIZATION OF LUNAR CONSEQUENCES OF FRAGMENTATION EVENTS INVOLVING NUCLEAR-POWERED SPACECRAFT IN THE CISLUNAR REGION

M. Nishiguchi, S. Bhadauria, and C. Frueh

School of Aeronautics and Astronautics, Purdue University, 701 W. Stadium Avenue, West Lafayette, IN 47907, USA,
Email: {mnishigu,sbhadaur, cfrueh}@purdue.edu

ABSTRACT

As interest in cislunar exploration grows, nuclear thermal propulsion (NTP) is emerging as a key technology for future missions. While NTP offers efficiency and high thrust-to-weight ratios, its safety risks remain a concern, particularly in the event of an in-space fragmentation. This paper investigates potential breakup events of an NTP-powered rocket near the Earth-Moon L_2 Lagrange point, analyzing debris dispersion and impact sites on the lunar surface. Additionally, we assess the observability of these fragments using space situational awareness (SSA) strategies. Furthermore, the potential radiation dose rate from nuclear-contaminated debris impacting the lunar surface is shown in the different scenarios. Our findings highlight the need for enhanced monitoring and mitigation measures to ensure the safe deployment of nuclear technology in cislunar space.

Keywords: Cislunar, Fragmentation, Nuclear Propulsion.

1. INTRODUCTION

Lunar exploration is accelerating, driven by national space agencies, private companies, and their growing partnerships [1]. The Artemis program exemplifies this renewed focus, aiming to return humans to the Moon and establish a sustainable presence. Additionally, the planned Lunar Gateway will serve as a key hub, providing power, propulsion, and habitation for extended cislunar missions [2].

As space missions extend beyond Earth, nuclear propulsion is emerging as a key technology for cislunar exploration. There are two main types: nuclear thermal propulsion (NTP), which heats liquid hydrogen for thrust, and nuclear electric propulsion (NEP), which generates electricity to power thrusters [3]. NTP is often preferred for human and scientific missions due to its higher thrust-to-weight ratio [4].

Despite its potential for future lunar missions, NTP is not a new concept. The U.S. developed the Nuclear Engine for Rocket Vehicle Application (NERVA) in the mid-20th century, successfully testing its feasibility. However, the program was discontinued in the 1970s due to budget constraints and shifting space priorities [5].

The Demonstration Rocket for Agile Cislunar Operations (DRACO) program, initiated by DARPA in 2021, advances NTP for agile cislunar maneuvering. In 2023, DARPA awarded contracts to Lockheed Martin and BWX Technologies to develop an NTP system, with an in-space demonstration planned for 2027 to support both military and civilian missions [6].

While nuclear propulsion offers significant advantages, safety remains a critical concern. Past incidents highlight the risks, such as the 1978 reentry of the Soviet Kosmos 954 satellite, which scattered radioactive debris over Canada due to a reactor failure. This event underscores the need for stringent safety measures to mitigate potential hazards [7].

In recent decades, multiple nations have advanced cislunar exploration through missions such as CNSA's Chang'e series [8], Israel's Beresheet lander [9], ISRO's Chandrayaan-3 [10], and NASA's CAPSTONE [11] and Artemis programs [12]. Alongside governmental efforts, private companies have also entered the cislunar domain with missions including Intuitive Machines' IM-1 and IM-2 [13], Firefly Aerospace's Blue Ghost [14], and iSpace's HAKUTO-R M1-3 [15]. With expanding cislunar operations, the risk of fragmentation events rises, posing threats to lunar and terrestrial assets, future missions, and potential settlements. While the cislunar satellite population remains low, past incidents, such as the 2022 Long March 3C booster collision with the Moon and the 2021 near-miss between NASA's Lunar Reconnaissance Orbiter and Chandrayaan-2 [16, 17], highlight the dangers. Studies suggest that cislunar fragmentation events can disperse debris widely, even reaching Earth or the Moon, emphasizing the need for enhanced monitoring and deeper insights into cislunar debris dynamics [18, 19]. Black and Frueh tackled this growing concern by developing a method to characterize fragmentation events through dynamical flow analysis, focusing on fragment behavior near the Earth-Moon L2 Lagrange point [20]. Similarly, Bhadauria et al. proposed an optimized sensor distribution strategy for cislunar space situational awareness (SSA) to track significant objects while considering potential unknown maneuvers at unpredictable times [21].

Given concerns about nuclear safety in space and the increasing risk of collisions in cislunar space, it is crucial to assess potential catastrophic events before deploying nuclear technology in cislunar and deep-space regions. One such event is the fragmentation of an NTP-powered rocket in cislunar space. Air Force Maj. Nate Greiner, DRACO program manager, stated that the reactor would not operate at high power until it reaches space, minimizing fission product accumulation before reaching a safe orbit beyond atmospheric reentry risk [22]. However, potential accidents in cislunar space remain unaddressed. This paper investigates breakup events in the cislunar region, particularly near the Earth-Moon L_2 Lagrange point, to estimate fragment dispersion, lunar impact locations, and observability using the Bhadauria et al. [21] method. We further assess the risks associated with nuclear-contaminated fragments impacting the lunar surface based on their radiation dose rates.

2. CHARACTERIZATION OF LUNAR IMPACTS

2.1. Circular Restricted Three Body Problem

In this study we use the CR3BP as a simplified, time-autonomous method that still captures the main dynamical structures. The governing equations for the spacecraft state are:

$$\ddot{x} - 2\dot{y} = \frac{\partial U^*}{\partial x} \quad \ddot{y} + 2\dot{x} = \frac{\partial U^*}{\partial y} \quad \ddot{z} = \frac{\partial U^*}{\partial z}. \quad (1)$$

Here, x, y, z, $\dot{x}$, $\dot{y}$, and $\dot{z}$ represent the position and velocity coordinates of the third body in the Earth-Moon rotating frame. In this frame, the x-axis is aligned with the vector pointing from Earth to the Moon, the z-axis is perpendicular to the Earth-Moon orbital plane, and the y-axis completes the right-handed orthonormal dextral triad [23]. U^* in the equations is called the pseudo-potential and is defined by:

$$U^* = \frac{1}{2}(x^2 + y^2) + \frac{(1-\mu)}{r_{ES}} + \frac{\mu}{r_{MS}}, \quad (2)$$

where r_{ES} and r_{MS} represent the distances of the satellite measured from the Earth and the Moon, respectively and $\mu = m2/(m1 + m2)$ is the non-dimensional mass parameter [23].

In the CR3BP, there is only one integral of motion, which is called Jacobi Constant (JC), and is defined by:

$$JC = 2U^* - (\dot{x}^2 + \dot{y}^2 + \dot{z}^2). \quad (3)$$

The JC is an energy-like quantity and the first and second terms represent potential and kinetic energy respectively.

2.2. Orbit Selection

L2 orbits have become preferred mission destinations because they offer communication coverage for the far side of the Moon and the lunar poles [24]. Additionally, the L2 point's strategic location acts as a gateway between the cislunar region and remote interplanetary destinations [25]. In this study, hypothetical fragmentation events are analyzed based on the number of fragments that impact the lunar surface. The first orbital family considered is the L_2 Lyapunov orbit family, which remains entirely within the CR3BP rotating plane. Additionally, the L_2 Halo orbit family is examined, which originates as a bifurcation from the planar L_2 Lyapunov orbits and extends into both the positive z (Northern) and negative z (Southern) directions. Figure 1 (a) and (b) show the selected orbits from L_2 Lyapunov and L_2 Halo orbital families for this paper, respectively. The plots are in an Earth-Moon rotational frame in which the origin is fixed at the barycenter of the Earth and the Moon and the axis is non-dimensionalized by dividing the dimensional distance by the distance between the two primary bodies. Table 1 shows the multidimensional initial position and velocity and JC for the selected orbits.

2.3. Debris Breakup Models

This paper presents the results of two case studies, each examining different models for the final state of fragments generated by an actual explosion in space. The two cases considered are: (1) Constant ΔV, where each fragment is assigned a fixed velocity change; (2) realistic Fragmentation, which accounts for a more physically realistic fragment distribution. Analogous to the constant ΔV analysis, we also performed constant JC cases, which constrains fragments to maintain the same JC value, because of the page count those results are not included here and are only referenced in the realistic fragmentation case.

The two fragmentation scenarios—the Constant ΔV and Constant JC cases—are physically unrealistic but serve as valuable tools for isolating key factors in fragment dynamics. The Constant ΔV scenario provides insight into how a uniform velocity perturbation influences fragment trajectories, while the Constant JC case allows for a controlled examination of fragment motion under a conserved dynamical constraint. Although realistic fragmentation events involve a complex distribution of energy and velocity variations, these simplified models offer a clearer understanding of individual effects. The insights gained from these cases provide a foundation for analyzing more realistic fragmentation scenarios.

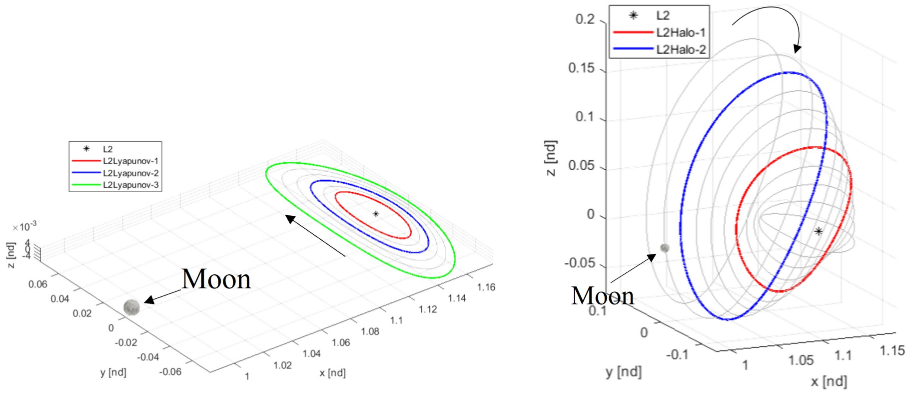

(a) L_2 Lyapunov (b) L_2 Halo

Figure 1. Selected orbits in (a) L_2 Lyapunov and (b) Halo orbital families for this study

Table 1. Initial State and Jacobi Constant for the Selected Orbits

Orbit Name	Initial Position [nd] [x, y, z]	Initial Velocity [nd] $[\dot{x}, \dot{y}, \dot{z}]$	JC
L_2 Lyapunov-1	[1.30168, 0 ,0]	[0, -0.57875, 0]	3.16967
L_2 Lyapunov-2	[1.17068, 0 ,0]	[0, -0.08697, 0]	3.16615
L_2 Lyapunov-3	[1.17818, 0 ,0]	[0, -0.13646, 0]	3.15695
L_2 Halo-1	[1.17342, 0 ,0.08]	[0,-0.18452, 0]	3.12579
L_2 Halo-2	[1.14220, 0 ,0.16]	[0,-0.22257, 0]	3.05970

2.4. Case 1: Constant ΔV

In the Constant ΔV case, all fragments experience a fixed velocity change due to the explosion, helping to assess how explosion magnitude affects the fragment distribution and lunar impacts. The direction of ΔV is determined by polar and azimuth angles, selected at constant intervals to evenly distribute fragments on a spherical surface. The final velocity of each fragment is given by:

$$\vec{v}_{f,k} = \vec{v}_{\text{sat}} + \Delta V \hat{v}_k \tag{4}$$

where $k = 1, 2, ..., n$ and n is the total number of fragments. In this study, three different values of $\Delta V(0.01\text{km/s}, 0.07\text{km/s}, \text{ and } 0.2\text{km/s})$ are considered. These values are chosen based on the result of the modified NASA Standard Breakup Model, which is discussed in Section 2.6. To be consistent, in this study, it is assumed that 250 fragments will be generated from a breakup event.

2.4.1. Investigation of L_2 Lyapunov Orbit

Figure 2 shows the distribution of the Number of Fragments Impacting the Lunar Surface (**NFILS**) along six L_2 Lyapunov orbits for different ΔV values. Note that to illustrate how the distribution of NFILs changes with orbit size, we present the distributions for all orbits shown in Figure 1, rather than limiting them to the colored ones. In the figure, blue indicates the fewest NFILs, while red represents higher numbers of NFILs. At $\Delta V = 0.01$ km/s, lower impact numbers (purple) appear on the far side of the orbit, while the highest NFILS in inner orbits occurs at higher y-coordinates. As orbit size increases, the highest impact region shifts toward the Moon-facing side. At $\Delta V = 0.07$ km/s, NFILS concentrates in the upper and lower segments (y-coordinate). At the highest ΔV, the NFILS pattern becomes less distinct, but the lowest NFILS remains on the Moon-facing side.

Figure 3 displays the highest NFILS locations in selected Lyapunov orbits for three ΔV values and their corresponding lunar impact sites. The green dot indicates the location that produces the highest NFILS on the displayed orbit, alongside the color coding from Fig. 2. To the right, the lunar surface is shown in longitude and latitude with the impacts from the green marked location as red stars. As ΔV increases, the impact region expands, but the total NFILS also rises compared to lower ΔV cases. Since L_2 Lyapunov orbits lie in the Earth-Moon orbital plane, and fragment perturbations have constant magnitude with a spherical distribution, the impact pattern on the lunar surface remains symmetric about the Moon's equator.

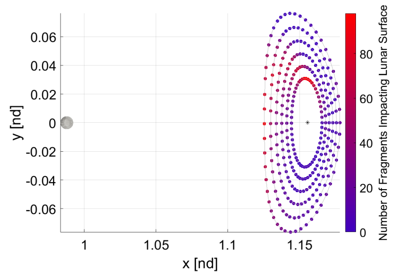

(a) $\Delta V = 0.01$ km/s

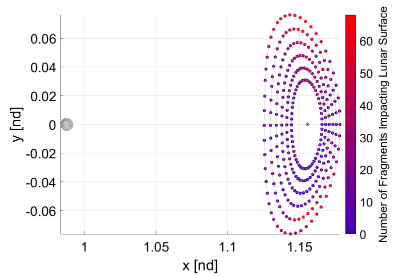

(b) $\Delta V = 0.07$ km/s

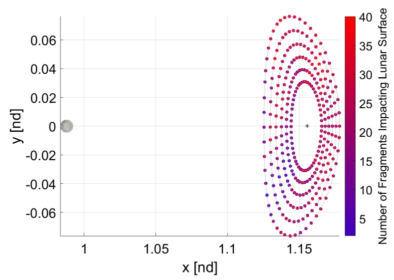

(c) $\Delta V = 0.2$ km/s

Figure 2. The Number of Fragments Impacting the Lunar Surface (NFILS) variations in L_2 Lyapunov family under constant ΔV fragmentations, with the moon dipicted on the left.

2.4.2. Investigation of L_2 Halo Orbit

The NFILS distribution under the three constant ΔV cases for the 11 L_2 Halo orbits is shown in Figure 4. As in Figure 2, we present the distributions for all orbits shown in Figure 1 (b), rather than limiting them to the selected ones. In the figure, the blue marks the fewest NFILs, and the red colors marks higher numbers of NFILS. Although these orbits are not co-planar with the Earth-Moon orbital plane, their NFILS distribution remains similar to that of L_2 Lyapunov orbits. For $\Delta V = 0.01$ km/s, the highest NFILS appears on the Moon-facing side, while for $\Delta V = 0.07$ km/s, it is concentrated in regions with larger y-coordinates. At $\Delta V = 0.2$ km/s, the highest NFILS remains near the upper and lower y-coordinates, though the trend is less distinct than in lower ΔV cases.

Figure 5 shows the locations of the highest NFILS in the selected Halo orbits for the three ΔV values with the corresponding impact locations on the lunar surface. The green dot indicates the location that produces the highest NFILS on the displayed orbit, alongside the color coding from Fig. 4. Since the orbits are not co-planar with the Earth-Moon orbital plane, unlike L_2 Lyapunov orbits, symmetry in the impact locations about the Moon's equator is no longer observed. However, the pattern of lunar impacts is more distinct for lower ΔV values, with the impact region expanding as the perturbation increases. This trend is also observed in L_2 Lyapunov orbits. Additionally, the shape of the lunar impact distribution on the map varies depending on the orbit size. This can be explained by the fact that the breakup location moves closer to the Moon as the orbit size increases in the Halo family, particularly in the southern part of the orbit.

2.5. Case 2: Realistic Fragmentations

The NASA Standard Breakup Model (SBM) is widely used for simulating fragmentation events but has limitations, including the lack of momentum conservation, velocity directionality, and mass optimization [26]. To address these gaps, Black and Frueh incorporated enhancements from other institutions, refining the model for their study [20]. This modified SBM is implemented in this study to simulate a realistic fragmentation event.

Figure 6 shows an example output of the modified SBM. A spacecraft with an NTP engine is assumed to have a total mass of 50,000 kg, including a 4,000 kg engine, based on literature [27, 28, 29]. The simulation generated 238 fragments with varying velocity perturbations. From the result of an example run of the modified SBM, the ΔV values investigated in the Constant ΔV case were chosen.

The process of simulating a realistic fragmentation involves running the modified SBM, propagating each fragment's state, and recording the lunar impact site locations and the total number of impacts. To account for statistical variations in the modified SBM, we repeat the process ten times for each breakup location. The number of fragments impacting the lunar surface (NFILS) in the distribution plots shown in Figure 7 and Figure 9 represents the average across these ten runs.

2.5.1. Investigation of L_2 Lyapunov Orbit

Figure 7 shows the average NFILS at each orbit location. At each point, ten simulations of realistic fragmentation were performed, and the average NFILS is color-coded, with red representing the largest NFILs and blue indicating the smallest NFILs in the orbit. In L_2 Lyapunov orbits, the highest NFILS typically occurs at higher y-coordinates, while for larger orbits, it also appears on the lower side. This distribution closely resembles the Constant ΔV case with $\Delta V = 0.07$ [km/s] in Figure 2. This similarity is expected, as $\Delta V = 0.07$ [km/s] was chosen

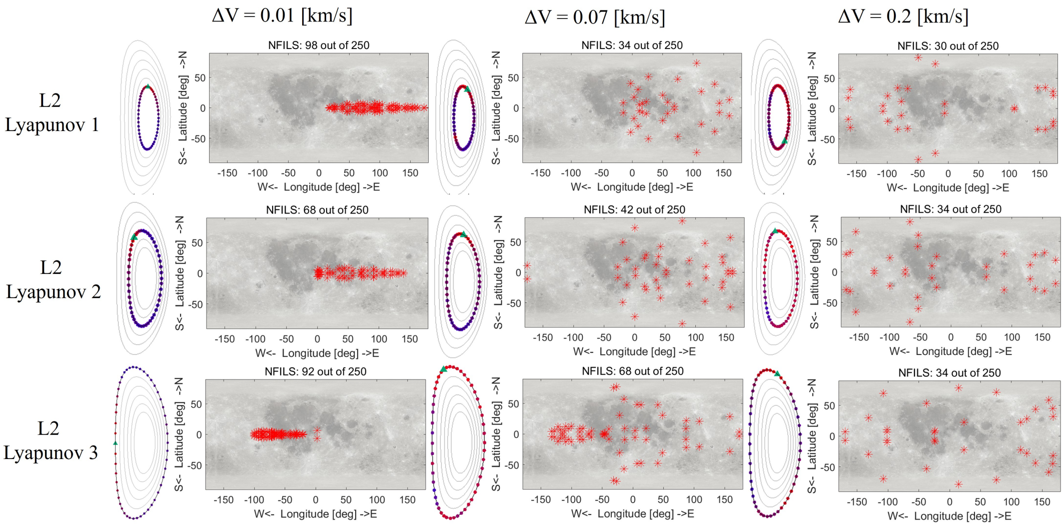

Figure 3. L_2 Lyapunov orbits for constant delta v cases: The green dot indicates the location that produces the highest NFILS on the displayed orbit, alongside the color coding from Fig. 2. To the right, the lunar surface is shown in longitude and latitude with the impacts from the green marked location as red stars.

for its proximity to the mean ΔV value in the modified SBM distribution shown in Figure 6.

Figure 8 highlights examples of realistic fragmentation in the selected L_2 Lyapunov orbits whose initial conditions are shown in Table 1 using the modified SBM. The top image shows the trajectories of both impacting and non-impacting fragments, while the bottom images illustrate the corresponding lunar impact sites (left) and the ΔV and J_C distribution of the generated fragments (right). The map of the impact site locations is overlaid with results from the constant ΔV and JC case simulations of fragmentation originated at the same location, along with the corresponding ΔV and JC distributions. Note that the impact locations are based on a single run and do not represent an average. The overlaid impact site map clearly shows that the impact pattern of the realistic fragmentation follows the impact pattern from the constant ΔV and JC cases, demonstrating the effectiveness of investigating hypothetical cases.

2.5.2. Investigation of the L_2 Halo Orbit

Figure 9 presents the same results as Figure 7 for L_2 Halo orbits. Ten simulations of realistic fragmentation were performed at each point, and the average NFILs is color-coded, with red representing the largest NFILs and blue indicating the smallest NFILs in the orbit. Larger orbits have fewer NFILS despite being closer to the Moon, while smaller orbits tend to show higher NFILS at the same orbital phase. This suggests that a greater tilt of the orbital plane increases the likelihood of fragments reaching the lunar surface.

Figure 10 illustrates examples of realistic fragmentation in the selected L_2 Halo orbits, with initial conditions provided in Table 1, using the modified SBM. The top image displays the trajectories of both impacting and non-impacting fragments, while the bottom images show the corresponding lunar impact sites (left) and the ΔV and J_C distribution of the generated fragments (right). Fragment trajectories appear more chaotic than in L_2 Lyapunov orbits due to the three-dimensional nature of the orbits.

3. VISIBILITY ANALYSIS

3.1. Parameterization of Visibility Constraints using Bi-circular Restricted Four Body Problem Geometry (BCR4BP)

To accurately assess illumination conditions for satellite surveillance, the Sun's position must be incorporated into the visibility model. This study employs the in-plane BCR4BP framework [30, 31, 32, 33] to parameterize the motion of the primary bodies—Earth (m_1), Moon (m_2), and Sun (m_4)—which influence target visibility in cislunar space. The mass of the Sun is set to be zero for this analysis to follow the dynamics of CR3BP. The BCR4BP describes the dynamics of an artificial satellite (m_3) under the gravitational effects of the Earth-Moon-Sun system. Further details on the model assumptions can be found in [21]. The repetitive geometry of the primary bodies in the BCR4BP enables an efficient visibility parameterization.

The position vectors $\vec{R}_{B_1 1}$ and $\vec{R}_{B_1 2}$, representing the Earth and Moon relative to the Earth-Moon Barycenter (B_1), are defined as:

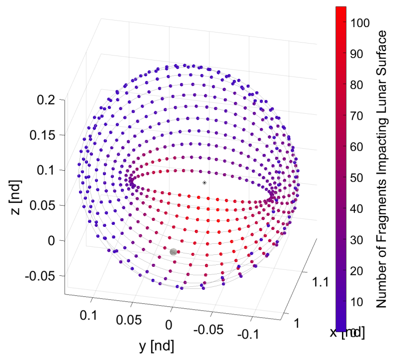

(a) $\Delta V = 0.01$ km/s

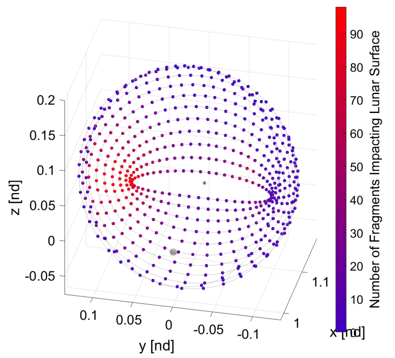

(b) $\Delta V = 0.07$ km/s

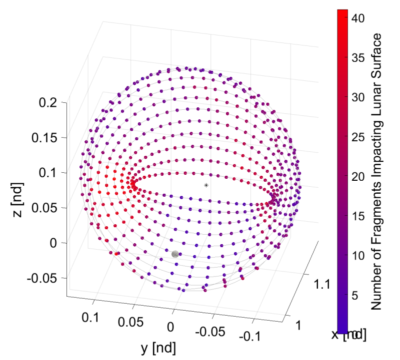

(c) $\Delta V = 0.2$ km/s

Figure 4. The Number of Fragments Impacting the Lunar Surface (NFILS) variations in L_2 Halo family under constant ΔV fragmentations, with the moon dipicted.

$$\vec{R}_{B_11} = |\vec{R}_{B_11}|(-\cos(\dot{\theta}t + \theta_0)\hat{X} - \sin(\dot{\theta}t + \theta_0)\hat{Y}), \tag{5}$$

$$\vec{R}_{B_12} = |\vec{R}_{B_12}|(\cos(\dot{\theta}t + \theta_0)\hat{X} + \sin(\dot{\theta}t + \theta_0)\hat{Y}). \tag{6}$$

Here, θ_0 and ϕ_0 denote the initial angles of the Moon and Sun relative to the inertial $\hat{X}$ axis, evolving with angular velocities $\dot{\theta}$ and $\dot{\phi}$, respectively.

The Sun's position relative to the Earth-Moon Barycenter (B_1) is derived using its angular velocity $\dot{\phi}$ with respect to the inertial $\hat{X}$ axis. The Earth-Moon Barycenter (B_1) position $\vec{R}_{B_2B_1}$ and the Sun's position $\vec{R}_{B_24}$ relative to the system Barycenter (B_2) are given by:

$$\vec{R}_{B_2B_1} = |\vec{R}_{B_2B_1}|(-\cos(\dot{\phi}t + \phi_0)\hat{X} - \sin(\dot{\phi}t + \phi_0)\hat{Y}), \tag{7}$$

$$\vec{R}_{B_24} = |\vec{R}_{B_24}|(\cos(\dot{\phi}t + \phi_0)\hat{X} + \sin(\dot{\phi}t + \phi_0)\hat{Y}). \tag{8}$$

By combining $\vec{R}_{B_24}$ and $\vec{R}_{B_2B_1}$, the Sun's position relative to the Earth-Moon Barycenter (B_1) is determined. These formulations based on BCR4BP parameters are advantageous for evaluating space-object's visibility.

3.2. Visibility Constraints

The optical constraints examined in this paper include exclusion angle zones from primary celestial bodies, i.e, the Sun, Moon, and Earth, and the telescope's limiting magnitude. More details on these constraints can be referred from Bhadauria et al. [21, 34] and are reiterated here for completeness.

3.2.1. Magnitude Constraint

The illumination of an object due to the sunlight can be computed as its visual magnitude [35, 21] and is expressed as

$$\text{mag}_{\text{object}} = \text{mag}_{\text{sun}} - 2.5\log_{10}(\frac{I_{\text{object}}}{I_{\text{sun}}}) \tag{9}$$

where mag_{sun} is the apparent reference magnitude of the Sun, I_{object} is the irradiance reflected off the spacecraft and I_{sun} is the Sun's reference irradiance. This paper assumes a cannonball model with a 1-meter radius and a Lambertian reflectivity of 0.5. A limiting magnitude constraint, denoted as $\text{mag}_{\text{limit}}$, is applied such that objects brighter than $\text{mag}_{\text{limit}}$ are visible, with a value of 18 chosen for this paper. The limiting magnitude depends on factors such as background noise, exposure time, atmospheric turbulence, image processing methods, and the optical system itself [36, 35, 37, 38].

$$V_{(\text{mag})} = \begin{cases} 1 \text{ if } \text{mag}_{\text{object}} < \text{mag}_{\text{limit}} \\ 0, \text{otherwise} \end{cases} \tag{10}$$

3.2.2. Exclusion Zones

Observations in the cislunar region are influenced by the relative positions of the Sun, Earth, and Moon with re-

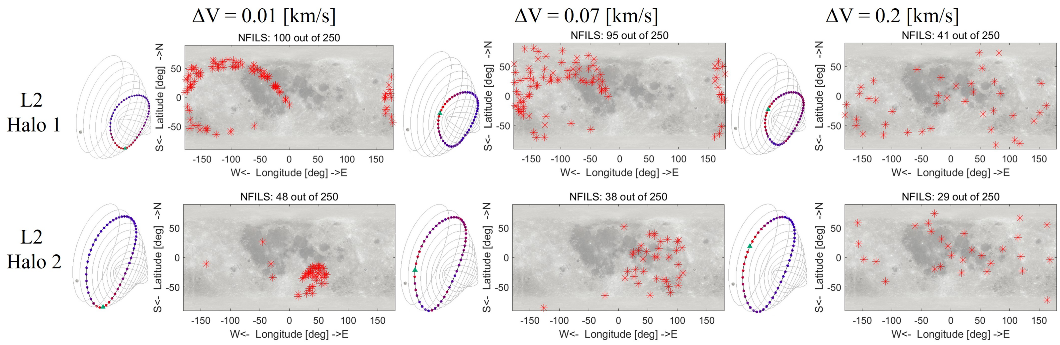

Figure 5. L_2 Halo orbits for constant delta v cases: The green dot indicates the location that produces the highest NFILS on the displayed orbit, alongside the color coding from Fig. 4. To the right, the lunar surface is shown in longitude and latitude with the impacts from the green marked location as red stars.

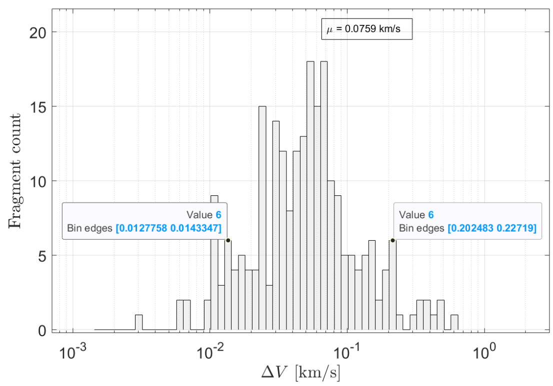

Figure 6. one run of the modified SBM, showing the fragmentation count as a function of ΔV

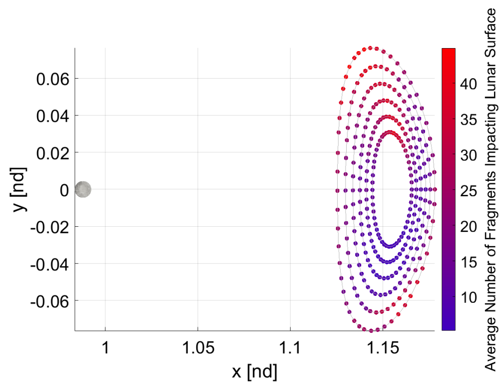

Figure 7. Distribution of the Number of Fragments Impacting the Lunar Surface (NFILS) under realistic fragmentation in L_2 Lyapunov orbits. At each point, 10 simulations of realistic fragmentation were performed, and the average NFILS at each point are reported.

spect to the object and the observer. Consequently, visibility constraints are defined by exclusion zones associated with these celestial bodies [21]. The exclusion angles with respect to Earth, Moon, and Sun define the exclusion zones and can be readily formulated in the BCR4BP [21]. The following table 2 lists the angle limits for defining the exclusion angle with respect to primaries and visibilities associated with them.

Primary body	**Angle limit**	**Visibility Constraints**
Earth	10°	$V_{(\mathrm{EEZ})} = \begin{cases} 1 \text{ if } \alpha > 10^\circ \\ 0, \text{otherwise} \end{cases}$
Moon	10°	$V_{(\mathrm{MEZ})} = \begin{cases} 1 \text{ if } \beta > 10^\circ \\ 0, \text{otherwise} \end{cases}$
Sun	30°	$V_{(\mathrm{SEZ})} = \begin{cases} 1 \text{ if } \gamma > 30^\circ \\ 0, \text{otherwise} \end{cases}$

Table 2. Exclusion angle zones with their thresholds and visibility constraints

The $V_{(\mathrm{EEZ})}$, $V_{(\mathrm{MEZ})}$ and $V_{(\mathrm{SEZ})}$ refer to visibility from the the Earth's exclusion zone (EEZ), Moon's exclusion zone (MEZ) and Sun's exclusion zone (SEZ), respectively.

3.2.3. Visibility Count Percentage

The visibility count percentage (VCP) quantifies an object's visibility over time as the percentage of time steps for which the object is observable. It can be computed for individual constraints (e.g., limiting magnitude, exclusion angles) or all constraints combined. Mathematically, VCP is given as [21]:

$$VCP = \frac{1}{n}\sum_{i=1}^{n}\frac{t_{\text{visible},i}}{t_{\text{all}}} \cdot 100, \tag{11}$$

where n is the number of observers, $t_{\text{visible},i}$ is the number of time steps the object is visible to the i^{th} observer, and t_{all} is the total number of time steps. VCP is computationally efficient and aids in generating visibility maps

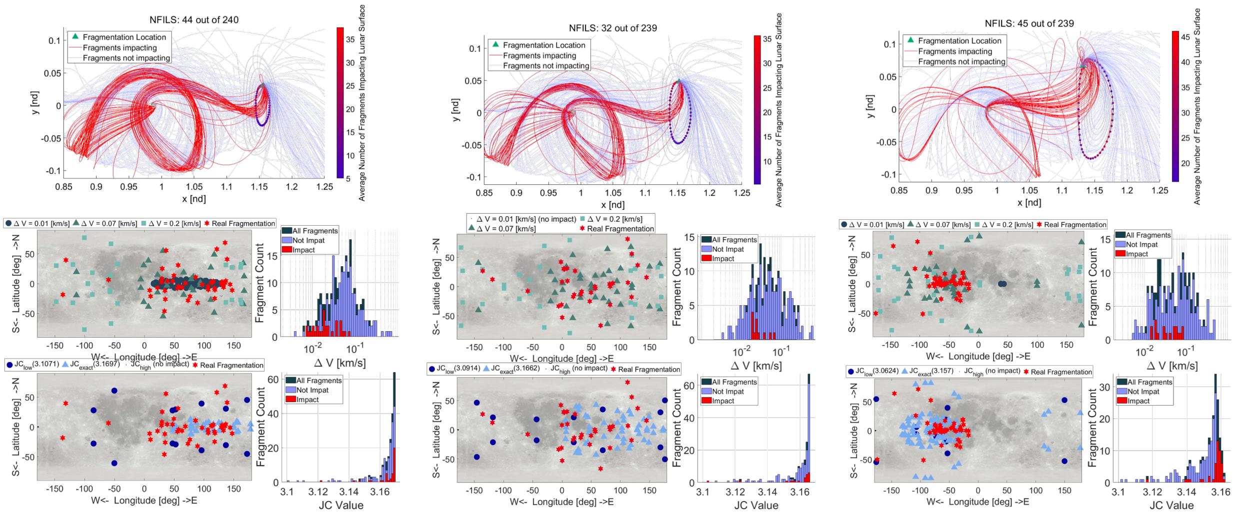

(a) L_2 Lyapunov 1 (b) L_2 Lyapunov 2 (c) L_2 Lyapunov 3

Figure 8. Examples of realistic fragmentation L_2 Lyapunov Orbits using the modified SBM. Top: trajectories of impacting/non-impacting fragments. Bottom Left: Lunar impacting site overlaid with the constant ΔV and JC simulation. Bottom Right: ΔV and JC distribution of the generated fragments

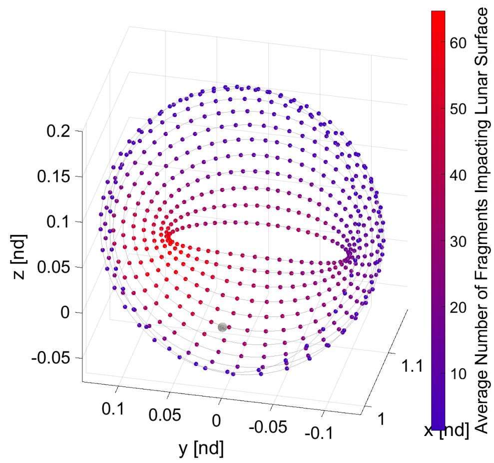

Figure 9. Distribution of the Number of Fragments Impacting the Lunar Surface (NFILS) under realistic fragmentation in L_2 Halo orbits. At each point, 10 simulations of realistic fragmentation were performed, and the average NFILS at each point are reported.

that can further be optimized with Particle Swarm Optimization (PSO) for optimal observer placement for maximum visibility. In this study, PSO is applied following Bhadauria et al. [21] to optimize observer placement in the cislunar region using visibility maps based on VCP. The objective function maximizes the number of visible objects from predefined observer locations:

$$f(r) = \bigcup_{i=1}^{n} (\text{objects visible by the } i^{th} \text{ observer}), \quad (12)$$

Where each observer's position is represented as:

$$r = \{r_{x1}, r_{y1}, r_{z1}, \ldots, r_{xi}, r_{yi}, r_{zi}\}. \quad (13)$$

Here, $\{r_{xi}, r_{yi}, r_{zi}\}$ defines the position of the i^{th} observer, constrained within 0.3 non-dimensional units around the Moon.

3.3. Constant ΔV: L_2 Lyapunov orbit with 0.01 km/s ΔV and 0.2 km/s ΔV

The location with the highest number of fragments impacting the Moon from a L_2 Lyapunov orbit, subjected to ΔV perturbations of 0.01 km/s and 0.2 km/s in 250 uniformly distributed directions, is analyzed for optimal average visibility using BCR4BP parameterization and PSO. For the L_2 Lyapunov orbit with these perturbations, only the trajectories hitting the Moon are mapped onto a set of preselected points in the Earth-Moon rotating frame. These points, uniformly distributed within a circular region of 0.25 non-dimensional units around the Moon, act as observers, while the mapped points represent the tracked objects.

Figure 11 shows the planar mapping of objects along with observers for an L_2 Lyapunov orbit subjected to 0.01 km/s and 0.2 km/s ΔV perturbations. The x-axis and y-axis represent the coordinate axes in the non-dimensional Earth-Moon rotating frame. The position of the Moon is marked by a black star. The equally spaced black and green points represent the observers, while the green points correspond to the mapped objects spanned by these perturbed orbits within a radial distance of 0.25 from the Moon. Figure 11 (a) and 11 (b) display the mapped objects for 0.01 km/s and 0.2 km/s ΔV perturbations, respectively. These mapped locations are used to assess

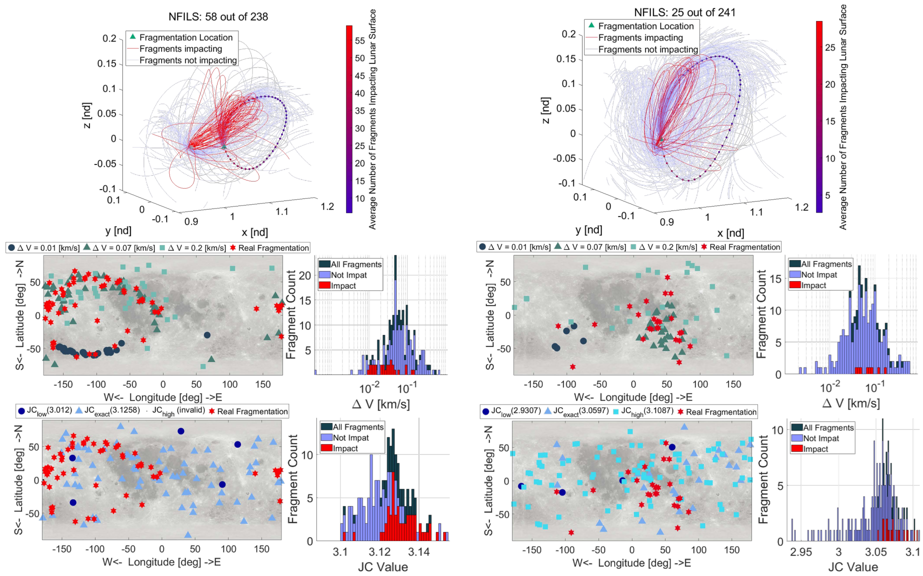

(a) L_2 Halo 1 (b) L_2 Halo 2

Figure 10. Examples of realistic fragmentation in L_2 Halo Orbits using the modified SBM. Top: trajectories of impacting/non-impacting fragments. Bottom Left: Lunar impacting site overlaid with the constant ΔV and JC simulation. Bottom Right: ΔV and JC distribution of the generated fragments

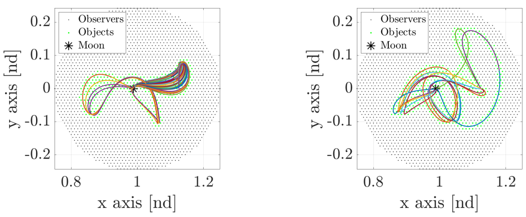

(a) (b)

Figure 11. Mapped points for visibility assessment of L_2 Lyapunov orbit perturbed with (a) 0.01 km/s ΔV and (b) 0.2 km/s ΔV

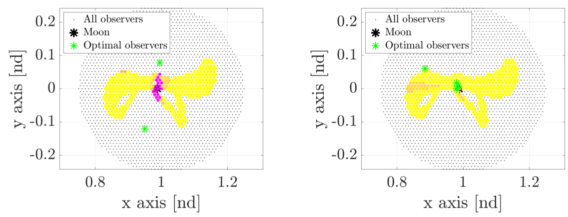

(a) (b)

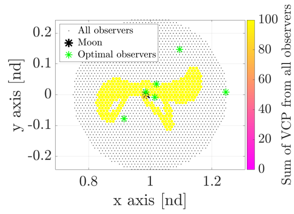

(c)

Figure 12. PSO plots for all mapped objects from L_2 Lyapunov orbit perturbed with 0.01 ΔV for 30 days with (a) two optimal observers, (b) four optimal observers, and (c) six optimal observers

the average visibility, which is subsequently employed to identify optimal observer positions through PSO. These optimal locations can then be compared to existing sensor trajectories, offering a straightforward quantitative method for evaluating their proximity to optimality.

Figure 12 illustrates the positions of optimal observers that maximize the number of visible objects while ensuring that the combined VCP from all observers remains above 80 percent. This optimization is performed using particle swarm optimization for a L_2 Lyapunov orbit with a ΔV of 0.01 km/s. A predefined set of locations serves as observer positions, while the mapped locations act as objects that the optimization process uses to satisfy the visibility requirement. The x-axis and y-axis correspond to the non-dimensional Earth-Moon rotating frame, with the Moon's position shown in black star. The colorbar represents the sum of VCP_{single} from all optimal observers for the mapped object locations. Figure 12(a) shows the optimal visibility achieved with two observers monitoring the region. Similarly, Figure 12(b) and Figure 12(c) depict configurations with four and six observers, respectively, to maximize visibility coverage. As the number of observers increases, the number of objects satisfying the condition $VCP > 80$ percent also increases.

Similar to Figure 12, the optimized cumulative VCP plots for a L_2 Lyapunov orbit with a ΔV of 0.2 km/s are illustrated in Figure 13. The axes, object parameters,

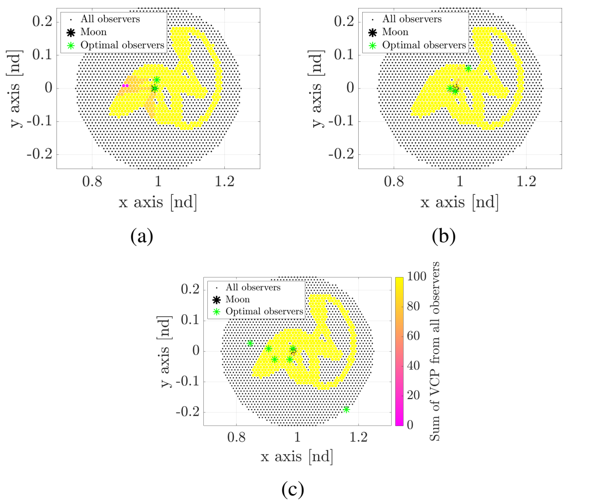

Figure 13. PSO plots for all mapped objects from L_2 Lyapunov orbit perturbed with 0.01 ΔV for 30 days with (a) two optimal observers, (b) four optimal observers, and (c) six optimal observers

visibility constraints, and optimization constraints remain consistent with those in Figure 12. Figure 13(a) depicts the optimal visibility configuration with two observers, Figure 13(b) with four observers, and Figure 13(c) with six observers.

3.4. Constant ΔV: L_2 Halo with 0.01 km/s ΔV and 0.2 km/s ΔV

The region with the highest concentration of fragments impacting the Moon, originating from a L_2 Halo orbit and subjected to ΔV perturbations of 0.01 km/s and 0.2 km/s in 250 uniformly distributed directions, is examined for optimal average visibility using BCR4BP parameterization and PSO. For the perturbed L_2 Halo orbits, only the trajectories that result in lunar impacts are mapped onto a predefined set of points in the Earth-Moon rotating frame. These points are uniformly distributed within a three-dimensional region of radius 0.2 non-dimensional units around the location, [1,0,0.05] for 0.01 km/s ΔV case and 0.2 non-dimensional units around the location, [1,0,0.05] for 0.2 km/s ΔV case as shown in Figure 14. They serve as observers (marked as black and green dots combined), while the mapped impact locations correspond to the tracked objects (marked as green dots). Figures 14 (a) and 14 (b) illustrate the mapped objects for ΔV perturbations of 0.01 km/s and 0.2 km/s applied to a L_2 Halo orbit, respectively. The axes and the location of Moon remain consistent with the ones in Figure 11. The visibility of these mapped objects is further optimized using the PSO,

Figure 15 depicts the optimal observer positions that maximize the number of visible objects while ensuring that the total VCP from all observers remains above 80 percent for a L_2 Halo orbit with a ΔV of 0.01 km/s. A

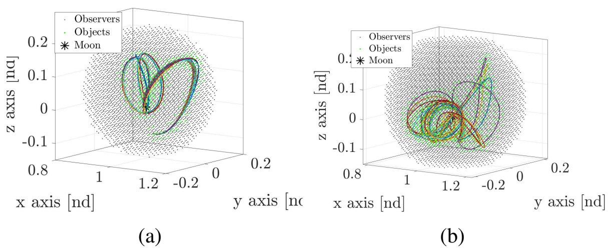

Figure 14. Mapped points for visibility assessment of L_2 Halo orbit with (a) 0.01 ΔV and (b) 0.2 ΔV

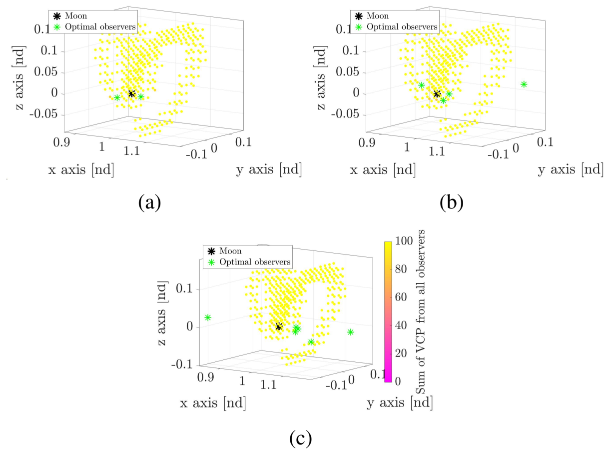

Figure 15. PSO plots for all mapped objects from L_2 Halo orbit perturbed with 0.01 ΔV for 30 days with (a) two optimal observers, (b) four optimal observers, and (c) six optimal observers

predefined set of locations serves as observer positions, while the mapped locations represent objects (shown in Figure 14 (a)) used in the optimization to satisfy the visibility criterion. The x-axis, y-axis, and z-axis correspond to the non-dimensional Earth-Moon rotating frame, with the Moon's position marked by a black star. The colorbar indicates the sum of VCP from all optimal observers for the mapped object locations. Figure 15(a) illustrates the optimal visibility achieved with two observers monitoring the region. Similarly, Figures 15(b) and 15(c) present configurations with four and six observers, respectively, to maximize visibility coverage. With six optimal observers, all the objects satisfy the condition $VCP > 80$ percent.

Similar to Figure 15, the optimized cumulative VCP plots for a L_2 Halo orbit with a ΔV of 0.2 km/s are illustrated in Figure 16. The axes, object parameters, visibility constraints, and optimization constraints remain consistent with those in Figure 12. The colorbar represents the sum of VCP across all optimal observers for the mapped object locations. Figure 16(a) depicts the optimal visibility configuration with two observers, Figure 16(b) with four observers, and Figure 16(c) with six observers. As the number of observers increases to six, all the objects satisfy the condition of a combined VCP

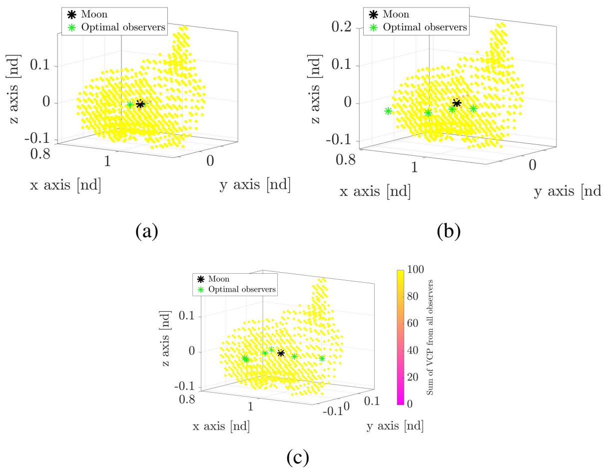

Figure 16. PSO plots for all mapped objects from L_2 Halo orbit perturbed with 0.2 ΔV for 30 days with (a) two optimal observers, (b) four optimal observers, and (c) six optimal observers

greater than 80 percent.

4. NUCLAER SAFETY ANALYSIS

4.1. Fission Products and Radiation Dose Simulation

Given the power of a reactor in a nuclear thermal propulsion (NTP), the rate of occurrence of the fission reaction can be computed by [39]:

$$\text{Fission Rate} \equiv \dot{F} = 5.4 \times 10^{23} \frac{P}{E_R}, \tag{14}$$

where P is the power of the reactor in Megawatts, and E_R is the recoverable energy of the engine and its value for U^{235} [s], is assumed to be 200 [MeV]. Thus, after operating the NTP engine with the power, P, for the total operation time, $t_{operation}$, the total number of fission reactions that occurred can be computed by[39]:

$$\begin{aligned}\text{Fission occurred} \equiv\ & F \\ =\ & \dot{F} \cdot t_{operation} \\ =\ & 5.4 \times 10^{23} \frac{P \cdot t_{operation}}{E_R}.\end{aligned} \tag{15}$$

Cumulative fission yields refer to the total yield of a particular fission product, accounting for both its direct production from nuclear fission and its indirect production from the radioactive decay of precursor isotopes. Thus, multiplying the number of fission events by the cumulative fission yield provides the number of atoms of a specific fission product.

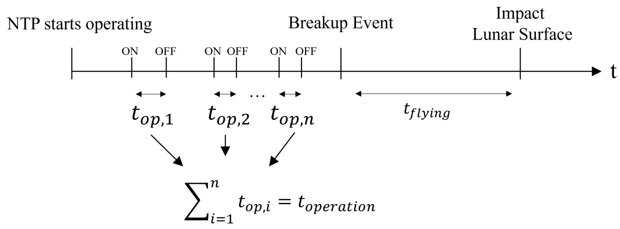

Figure 17. Timeline for the nuclear safety analysis. $t_{op,n}$ denotes the duration of the nth burn of NTP before the breakup event. The total burn time of the NTP is represented as the NTP operation time denotes as $t_{operation}$. The time between the breakup event and the lunar impact of a fragment is denoted as t_{flying}.

Since the fragmentation events are assumed to occur in a periodic orbit near the L_2 Lagrange point, the operation time for the NTP engine is based on lunar mission planning literature [40, 27, 41]. Specifically, the total operation time is assumed to be 1800 seconds, considering only the one-way trip to the Moon and not the return journey to Earth. To simplify the calculation, the decay of the fission product is assumed to start right after the breakup event. The number of atoms of a fission product after time, t, can be modeled as:

$$N(t) = N_0 e^{-\lambda t}, \tag{16}$$

where N_0 is the initial number of atoms, $\lambda = 0.693/t_{0.5}$, and $t_{0.5}$ is the half-life of the fission product. To analyze the dose rate from nuclear-contaminated fragments impacting on the lunar surface, the time, t, in Equaion 16 is assumed to be the time between the breakup event and the impact on the lunar surface, t_{flying}. Figure 17 illustrate the definitions of $t_{operation}$ and t_{flying}. $t_{op,n}$ denotes the duration of the nth burn of NTP before the breakup event. The total burn time of the NTP is represented as the NTP operation time denotes as $t_{operation}$. The time between the breakup event and the lunar impact of a fragment is denoted as t_{flying}.

From the simulation of realistic fragmentation events, t_{flying} is found to range between 1.0×10^5 s and 1.0×10^6 s. Therefore, to estimate the radiation dose rate due to fragments from a rocket equipped with a nuclear thermal propulsion system in the cislunar region, the flight time, t_{flying}, is assumed to be 5×10^5 s (approximately 5.79 days).

Radioactivity is the spontaneous emission of radiation from the unstable nucleus of an atom as it undergoes decay, releasing alpha, beta, or gamma radiation to achieve a more stable state. The radioactivity, Q, can be computed from the decay constant, λ and the number of atoms, N, as [42]:

$$Q = \lambda N(t)[Bq] = 10^{-6} \cdot \lambda N(t)[MBq]. \tag{17}$$

Effective dose rate is the rate at which an individual re-

Table 3. The effect of radiation on the human body [46]

Radiation Doses	Effects
10 [Sv]	Death within weeks
3 [Sv]	Survival rate approximately 50 %
1 [Sv]	Causes radiation sickness and nausea.
0.7 [Sv]	Vomiting, hair loss within 2-3 weeks
0.1 [Sv]	Lowest dose linked to cancer risk

ceives an effective dose of radiation over time and is used to assess radiation exposure risks and ensure compliance with safety limits. The effective dose rate observed at a distance r from a radioactive material with activity Q can be computed by [43]:

$$\dot{E} = \frac{\Gamma Q}{r^2}[\mu Sv/h], \quad (18)$$

where Γ is the effective dose rate constant with units of $[\mu\text{Sv} \cdot \text{m}^2 \cdot \text{MBq}^{-1} \cdot \text{h}^{-1}]$. The effective dose rates for all fission products are summed up and reported as the total dose rate in the following results.

4.2. Radiation Dose rate due to the nuclear-contaminated fragments

To compute the radioactivity of one of the 250 fragments, it is assumed that all fission products generated by the reactor are attached to fragments associated with the NTP engine. The number of atoms of fission products attached to a fragment from the NTP engine is then scaled by dividing the total number of atoms by $250 \times \frac{4000kg}{50000kg}$, where 250 is the number of fragments, 4000 kg is the mass of the rocket system, and 50,000 kg is the total mass of the spacecraft. Thus, by Equation 17 and the scaling factor, the radioactivity of a nuclear-contaminated fragment is computed. Then, Equation 18 is applied to the radio activity of a nuclear-contamintated fragment to compute the radiation dose rate due to the fragment at each distance.

Figures 18 to 20 illustrate the dose rate from a nuclear-contaminated fragment of a nuclear reactor, simulated by varying three independent variables: reactor power, $t_{operation}$, and t_{flying}. The results are compared with the natural space radiation on the lunar surface (5.7042×10^{-5} Sv/h) [44] and the peak dose rate recorded during the 2011 Fukushima Daiichi nuclear disaster, one of the most severe nuclear accidents in recent history (300 Sv/h) [45]. Table 3 presents the effects of radiation exposure on the human body. While the values in the table cannot be directly compared with the plot, as the plot shows the dose rate rather than the total dose, it provides context for understanding the potential consequences to the human body.

Figure 18 shows the relationship between the reactor power and the radiation dose rate due to the nuclear-contaminated fragment. The three values for the reactor power (300, 500, and 700 [MW]) were chosen based on the values reported in literature [47, 48, 49]. The result indicate that the radiation dose rate from a nuclear-contaminated fragment exceeds the natural space radiation on the lunar surface within an area of approximately 600–800 m immediately after the impact. At the impact site, the radiation dose rate exceeds the peak dose rate recorded after the Fukushima Daiichi nuclear disaster.

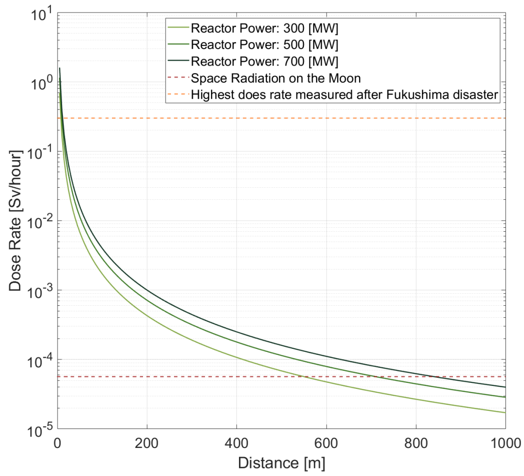

Figure 18. Radiation dose rate from a nuclear-contaminated fragment: Reactor power variation with a flight time of $t_{flying} = 5.79$ days and operational time of $t_{operation} = 1800$ s.

As time progresses, the radioactive material decays, leading to a decrease in radioactivity. Figure 19 illustrates the variation in radiation dose rate over time for a scenario involving a reactor power of 500 MW with $t_{operation} = 1800s$ where the cases of $t_{flying} =$ 1 week, 1 month, 6 month, and 1 year are plotted. Even one year after the impact, the radiation dose rate at the impact site remains more than ten times higher than the natural space radiation on the lunar surface. Therefore, leaving the nuclear-contaminated fragments at the impact site would not resolve the problem in a short time period.

Given the risk of nuclear-contaminated fragments impacting the lunar surface and polluting the lunar environment, there is a trade-off between shortening mission time with NTP and the increased risk of contamination due to higher fission product production. Figure 20 shows the variation in radiation dose rate under different operation times involving a reactor power of 500 MW with $t_{flying} = 5.79$ days. It turns out that even with just 1 second of operation, the radiation dose at the impact site immediately after impact exceeds the natural space radiation on the lunar surface. Therefore, in mission planning for NTP-based missions, the operation time must be determined not only from a trajectory perspective but also by considering the risk of nuclear contamination—especially in regions where humans may be present on the Moon.

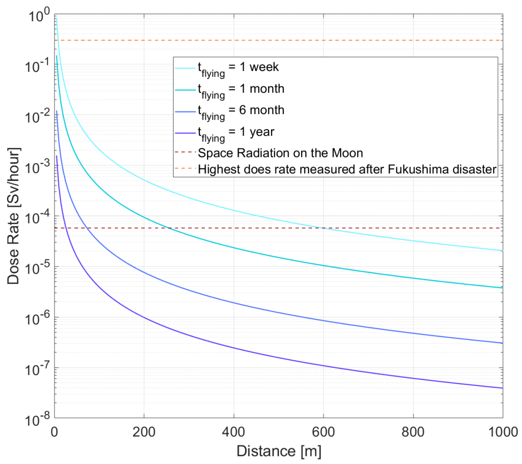

Figure 19. Radiation dose rate from a nuclear-contaminated fragment: Variation of t_{flying} with reactor power of 500 MW and $t_{operation} = 1800$ s.

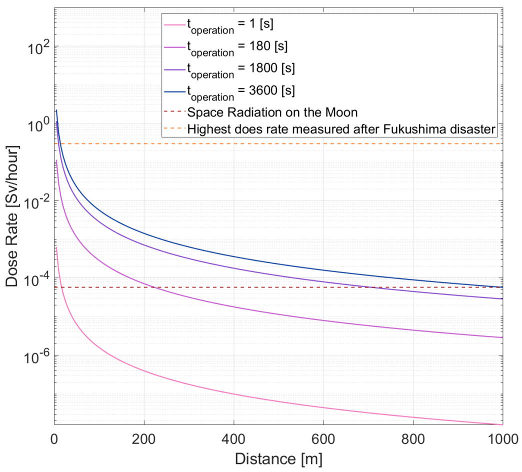

Figure 20. Radiation dose rate from a nuclear-contaminated fragment: Varying $t_{operation}$ with reactor power of 500 MW and $t_{flying} = 5.79$ days.

4.3. Challenges of Decontamination in the Lunar Environment

Figure 21 illustrates the distribution of fragments on the lunar surface, simulated for the realistic fragmentation case of L_2 Halo-1, as presented in Figure 10(a). The right panel provides a close-up of a high-density region. Assuming all fragments within the close-up window are nuclear-contaminated, the blue line marks the boundary where the radiation dose rate from the fragment (indicated by the red dot) equals the natural space radiation on the Moon. If contaminated fragments impact within a confined region, the cumulative radiation at the impact site would be the sum of the radiation dose rates from each fragment. From a radiation safety perspective, a more dispersed impact pattern would be preferable, as it minimizes localized radiation exposure.

However, this analysis assumes fragments land intact. In reality, impacts would likely shatter them, dispersing radioactive material into the regolith. Due to the Moon's low gravity, the disturbed regolith would remain suspended longer, complicating decontamination. Conventional Earth-based methods, such as water washing or nano-bubble technology [50], are impractical on the Moon due to limited resources. From a decontamination perspective, a more confined impact pattern would be preferable, reducing the logistical challenges of cleanup.

These conflicting priorities highlight the need to study impact distributions and develop efficient, low-intervention decontamination strategies for the lunar environment.

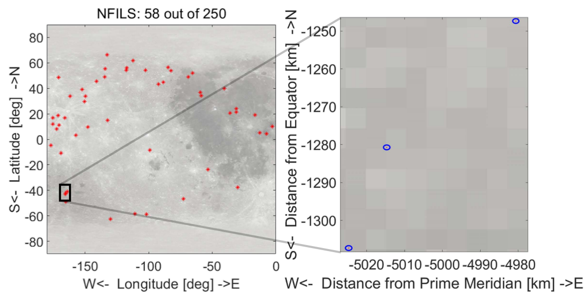

Figure 21. Distribution of Nuclear-Contaminated Objects on the lunar surface simulated in the realistic fragmetation case for L_2 Halo-1, and a close-Up of a High-Density Region. The blue line shows the locaiton at which the radiation dose rate from the fragment located at the red dot is equal to the natural space radiation on the moon.

5. CONCLUSIONS

This study examined the impact distributions of fragments in L_2 Lyapunov and Halo orbits under the hyphthetical constant ΔV case and the realistic fragmentation modeled by the modified SBM. The results indicate that lower ΔV values produce more concentrated impact regions, whereas higher ΔV leads to fewer total impacts as more fragments escape lunar gravity in the investigated cases. In Halo orbits, orbital tilt, and size further influence NFILS, with increased z-coordinate variations reducing the number of impacts.

Additionally, this work identifies key impact regions and optimizes surveillance using electro-optical space-based sensors. A visibility count percentage (VCP) is introduced to quantify regional visibility based on user-defined constraints and object parameters. The BCR4BP parameterization with Particle Swarm Optimization (PSO) determines optimal observer placements for perturbed L_2 Lyapunov and Halo orbits under constant ΔV and Jacobi cases. A constellation of two to six observers is analyzed over 30 days, demonstrating that while two observers cannot ensure full custody, optimal placement maximizes coverage. With six optimally placed observers, near-total custody is achievable despite visibility constraints. Increasing the number of observers significantly enhances object detection, providing insights into the design of surveillance constellations for full coverage.

Furthermore, results indicate that nuclear-contaminated fragments from an NTP system can generate radiation levels significantly exceeding natural lunar background radiation, affecting areas up to 800 m from the impact site. Even a year post-impact, radiation levels remain substantially elevated, highlighting the long-term contamination risk. Consequently, mission planning for NTP-based systems must balance trajectory optimization with the potential for nuclear contamination, particularly in regions with human activity on the Moon.

ACKNOWLEDGMENTS

The authors would like to express their gratitude to Dr. Arly Black for laying the foundation of this study, particularly in developing the breakup model and characterizing fragmentation dynamics. Special thanks also go to Yusuke Ota and Paul Stockette for their invaluable advice on the nuclear safety analysis aspect of this project. Their insights and expertise greatly contributed to the depth and rigor of this work.

REFERENCES

1. A. Melamed, A. Rao, O. de Rohan Willner, and S. Kreps, "Going to outer space with new space: The rise and consequences of evolving public-private partnerships," *Space Policy*, vol. 68, p. 101626, 2024.
2. E. Lehnhardt, J. Olansen, S. Fuller, D. Connell, J. Mason, T. Travis, and C. Fleming, "Gateway Program Development Progress," in *IAF Human Spaceflight Symposium*, (Milan, Italy), pp. 78–83, International Astronautical Federation (IAF), 2024.
3. S. W. Paek, E. S. Park, S. Brooks, and R. Roy, "Sustainability considerations of nuclear power in space transportation and infrastructures," Aug. 2024.
4. D. Thomas, "Nuclear thermal propulsion – Progress and potential," *Journal of Space Safety Engineering*, vol. 11, pp. 362–373, June 2024.
5. P. Pempie, "HISTORY OF THE NUCLEAR THERMAL ROCKET PROPULSION," 2002.
6. "NASA, DARPA Partner with Industry on Mars Rocket Engine - NASA — nasa.gov." https://www.nasa.gov/technology/nasa-darpa-partner-with-industry-on-mars-rocket-engine/, 2023. [Accessed 21-03-2025].
7. M. Pietkiewicz, "THE "LIABILITY CONVENTION" IN A CLASH WITH PRACTICE – EXAMPLE OF THE "KOSMOS 954" SATELLITE," *Studia Iuridica*, pp. 54–69, Sept. 2023.
8. C. Li, W. Zuo, W. Wen, X. Zeng, X. Gao, Y. Liu, Q. Fu, Z. Zhang, Y. Su, X. Ren, F. Wang, J. Liu, W. Yan, X. Tan, D. Liu, B. Liu, H. Zhang, and Z. Ouyang, "Overview of the Chang'e-4 Mission: Opening the Frontier of Scientific Exploration of the Lunar Far Side," *Space Science Reviews*, vol. 217, p. 35, Mar. 2021.
9. "Beresheet nasa science." https://science.nasa.gov/mission/beresheet/. [Accessed 23-03-2025].
10. "Chandrayaan-3 details." https://www.isro.gov.in/Chandrayaan3_Details.html. [Accessed 24-03-2025].
11. "What is capstone? nasa." https://www.nasa.gov/smallspacecraft/capstone/. [Accessed 24-03-2025].
12. "Artemis nasa." https://www.nasa.gov/humans-in-space/artemis/. [Accessed 24-03-2025].
13. "Im-1 intuitive machines." https://www.intuitivemachines.com/im-1. [Accessed 24-03-2025].
14. "Blue ghost firefly aerospace." https://fireflyspace.com/blue-ghost/. [Accessed 24-03-2025].
15. "Missions ispace." https://ispace-inc.com/missions. [Accessed 24-03-2025].
16. M. Wall, "Rogue rocket that slammed into the moon last year confirmed to be Chinese vehicle — space.com." https://www.space.com/moon-crash-march-2022-china-rocket-body, November 2023. [Accessed 23-03-2025].
17. J. Foust, "Foust Forward — Keeping cislunar space safe." https://spacenews.com/foust-forward-keeping-cislunar-space-safe/, June 2023. [Accessed 23-03-2025].
18. A. Black and C. Frueh, "Investigation of fragmentation events in the cislunar domain," in *33rd AAS/AIAA Space Flight Mechanics Meeting, Austin, TX*, 2023.
19. P. Guardabasso, D. K. Skoulidou, L. Bucci, F. Letizia, S. Lemmens, M. Ansart, X. Roser, S. Lizy-Destrez, and G. Casalis, "Analysis of accidental spacecraft break-up events in cislunar space," *Advances in Space Research*, vol. 72, no. 5, pp. 1550–1569, 2023.
20. A. Black and C. Frueh, "Fragmentation characterization in the circular restricted three body problem for cislunar space domain awareness," *Advances in Space Research*, 2024. Submitted, under review.
21. S. Bhadauria, A. Black, and C. Frueh, "Cislunar Surveillance Optimization and Key Region Identification," in *2024 Advanced Maui Optical and Space Surveillance Technologies Conference (AMOS)*, 2024.

22. J. Harper, "DARPA Set to Deliver New Space Capabilities," 2025.
23. K. Howell, *AAE 632 Advanced Orbital Dynamics*. School of Aeronautics and Astronautics, Purdue University, 2018.
24. R. W. Farquhar, *The utilization of halo orbits in advanced lunar operations*, vol. 6365. National Aeronautics and Space Administration, 1971.
25. T. Swenson, M. Lo, B. D. Anderson, and T. Gorordo, "The topology of transport through planar lyapunov orbits," in *2018 Space Flight Mechanics Meeting*, p. 1692, 2018.
26. N. Johnson, P. Krisko, J.-C. Liou, and P. Anz-Meador, "Nasa's new breakup model of evolve 4.0," *Advances in Space Research*, vol. 28, no. 9, pp. 1377–1384, 2001.
27. M. Duchek, C. Harnack, D. Nikitaeva, and S. Greenhalge, "KEY PERFORMANCE PARAMETERS FOR AN OPERATIONAL CIS-LUNAR NTP VEHICLE,"
28. O. Gonzalez-nunez, "Demonstration rocket for agile cislunar operations (draco) nuclear thermal rocket (ntr) program's reactor transportation support." https://usfcr.com/search/opportunities/?oppId=f303556536d54563995ef6e9fa3be189. [Accessed 18-03-2025].
29. S. Kumar, L. D. Thomas, and J. T. Cassibry, "Application of nuclear thermal propulsion for sustainable cislunar exploration," *Acta Astronautica*, vol. 228, pp. 435–441, Mar. 2025.
30. R. Broucke, "Stability of periodic orbits in the elliptic, restricted three-body problem.," *AIAA journal*, vol. 7, no. 6, pp. 1003–1009, 1969.
31. V. Szebehely and F. Geyling, "Theory of orbits: The restricted problem of three bodies," 1968.
32. M. Hénon, "Generating families in the restricted three-body problem; number 52 in lecture note in physics. monographs," 1997.
33. A. Lemaître, "High-order resonances in the restricted three-body problem," *Celestial mechanics*, vol. 32, no. 2, pp. 109–126, 1984.
34. S. Bhadauria and C. Frueh, "Optical observation regions in cislunar space using the bi-circular restricted four body problem geometry," in *2022 Advanced Maui Optical and Space Surveillance Technologies Conference (AMOS)*, 2022.
35. C. Frueh, "Lecture notes of the course aae590: Space traffic management,purdue university," Fall 2023.
36. C. Frueh, B. Little, and J. McGraw, "Optical sensor model and its effects on the design of sensor networks and tracking," in *Advanced Maui Optical and Space Surveillance Technologies Conference (AMOS)*, sep 2019.
37. F. Sanson and C. Frueh, "Noise Quantification in Optical Observations of Resident Space Objects for Probability of Detection and Likelihood," in *AAS/AIAA Astrodynamic Specialist Conference, Vail, CO*, 2015. 15-634.
38. F. Sanson and C. Frueh, "Noise estimation and probability of detection in nonresolved images: Application to space object observation," *Advances in Space Research*, vol. 64, pp. 1432 – 1444, 2019.
39. J. Lamarsh, *Introduction to Nuclear Reactor Theory*. American Nuclear Society, 2002.
40. J. H. Altseimer, G. F. Mader, and J. J. Stewart, "Operating Characteristics and Requirements for the NERVA Flight Engine," *Journal of Spacecraft and Rockets*, vol. 8, pp. 766–773, July 1971.
41. Sahil Umarani, "A Comprehensive Review on Nuclear Thermal Propulsion System: Solid Core Design," *Acceleron Aerospace Journal*, vol. 3, pp. 688–703, Nov. 2024.
42. J. R. Lamarsh and A. J. Baratta, *Introduction to nuclear engineering*. Addison-Wesley series in nuclear science and engineering, Upper Saddle River, N.J: Prentice Hall, 3rd ed ed., 2001.
43. B. Lauridsen, "TABLE OF EXPOSURE RATE CONSTANTS AND DOSE EQUIVALENT RATE CONSTANTS,"
44. S. Zhang, R. F. Wimmer-Schweingruber, J. Yu, C. Wang, Q. Fu, Y. Zou, Y. Sun, C. Wang, D. Hou, S. I. Böttcher, S. Burmeister, L. Seimetz, B. Schuster, V. Knierim, G. Shen, B. Yuan, H. Lohf, J. Guo, Z. Xu, J. L. Freiherr Von Forstner, S. R. Kulkarni, H. Xu, C. Xue, J. Li, Z. Zhang, H. Zhang, T. Berger, D. Matthiä, C. E. Hellweg, X. Hou, J. Cao, Z. Chang, B. Zhang, Y. Chen, H. Geng, and Z. Quan, "First measurements of the radiation dose on the lunar surface," *Science Advances*, vol. 6, p. eaaz1334, Sept. 2020.
45. Internationale Atomenergie-Organisation, ed., *The Fukushima Daiichi accident*. STI/PUB, Vienna, Austria: International Atomic Energy Agency, 2015.
46. "Radioactivity measurements — aktinovolia.com." https://aktinovolia.com/measurement-radioactivity-radiation/. [Accessed 20-03-2025].
47. P. Venneri and Y. Kim, "Advancements in the Development of Low Enriched Uranium Nuclear Thermal Rockets," *Energy Procedia*, vol. 131, pp. 53–60, Dec. 2017.
48. G. J. Youinou and A. Abou-Jaoudé, "Preliminary Conceptual Design of Nuclear Thermal Rocket Reactor Cores Using Ceramic Fuels with Beryllium or Composite Neutron Moderators," *Nuclear Science and Engineering*, vol. 198, pp. 1534–1565, Aug. 2024.
49. C. R. Joyner, D. J. Levack, T. Jennings, M. Eades, and V. Patel, "Engine Design Attributes Relative to HEU and LEU Core Approaches for a Small Thrust NTP," in *52nd AIAA/SAE/ASEE Joint Propulsion Conference*, (Salt Lake City, UT), American Institute of Aeronautics and Astronautics, July 2016.
50. J. Semmler, Y. Yao, K. Volchek, P. Lambert, C. E. Brown, T. Mahilrajan, and M. McCall, "ASSESSMENT OF DECONTAMINATION, DECOMMISSIONING, AND REMEDIATION METHODOLOGIES AT FUKUSHIMA," 2014.